

Mode I steady-state crack propagation through a fully-yielded ligament in thin ductile metal foils



Wade R. Lanning^a, Camilla E. Johnson^a, Syed Saad Javaid^{a,b}, Christopher L. Muhlstein^{a,*}

^a School of Materials Science and Engineering, Georgia Institute of Technology, USA

^b National University of Sciences and Technology, Islamabad, Pakistan

ARTICLE INFO

Keywords:

Steady-state crack growth
Fracture toughness
Thin sheet
Ductile tearing
Stable crack growth
Fracture mechanics

ABSTRACT

Steady-state crack propagation is the advance of a self-similar crack tip with a constant driving force. Though steady-state growth is often described with analytical models, it is rarely experimentally observed or characterized under quasi-static loading conditions. Thin ductile metal sheets, such as the 25.4 μm, 50.8 μm, and 127 μm thick 1235 aluminum specimens used in this study, exhibit steady-state crack propagation but cannot be characterized by conventional linear-elastic (K) or elastic-plastic (J) crack tip parameters that require contained crack tip plastic zones. Instead we used a fully-yielded plastic crack growth resistance analysis (i.e., ligament stresses were above the tensile yield stress) to identify when cracks in thin aluminum sheet specimens reached steady-state propagation conditions. At steady-state a constant, characteristic crack growth resistance, σ_c was observed for each sheet thickness ($\sigma_{c25.4 \mu m} = 60$ MPa, $\sigma_{c50.8 \mu m} = 95$ MPa, and $\sigma_{c127 \mu m} = 93$ MPa). This σ_c -controlled crack growth is dramatically different from conventional linear elastic and elastic plastic crack growth because the plastic zone is uncontained and extends across the remaining ligament.

1. Introduction

Steady-state crack growth is the propagation of a crack with a fracture process zone that does not change as the crack grows [1,2] and the corresponding driving force to propagate the crack remains constant [3]. Steady-state crack propagation is a special case where the driving force for crack advance and material crack growth resistance both converge to some constant value as a crack advances. This convergence may occur under quasi-static crack growth conditions [1,3,2,4] or time-dependent deformation conditions due to dynamic crack growth [5] or creep crack growth [6–9].

Classic descriptions of quasistatic, mode I steady-state crack growth presume that the plastic zone remains well-contained and near the crack tip [1,3,7]. Typical crack growth resistance measurements in metals impose limitations on plastic zone size by using large specimens for K or J analyses [2,4] or double edge notch specimens for essential work of fracture [2,10,11] analyses. Steady-state creep growth involves a low driving force for crack propagation, which confines the most extensive deformation to the near-crack tip region [7,9]. Standard metal sheet tearing resistance measurements characterize mode III crack growth, which limits plasticity because a large portion of the un-torn ligament remains completely stress free [12]. All of these

established measurements and descriptions of steady-state crack growth involve a limited plastic zone size. Specifically, a self-similar crack tip process zone which is embedded inside a contained, self-similar plastic zone which is in turn embedded inside an elastic deformation field. A well-defined and contained plastic zone based on strategies such as the Hutchinson, Rice, Rosengren (HRR) field helps ensure valid K and J -based characterization of crack growth, but it is *not* a prerequisite for steady-state crack growth or a fundamental restriction on the calculation of the J -integral.

In a prior publication [13] we found that a single parameter, σ_c , characterized mode I crack growth resistance in thin (25.4 μm) aluminum sheets. Even though those specimens showed extensive plastic deformation, crack propagation was controlled by a characteristic driving force σ_c , which indicated steady-state crack growth. In contrast to conventional descriptions of steady-state crack growth [1,3,7,2,4], propagation stress (or net section stress) analyses of mode I crack propagation require a fully-yielded uncracked ligament (i.e., stresses in the ligament are above the tensile yield stress). Fig. 1 schematically shows the different stress vs. normalized crack length responses of hypothetical σ_c -controlled [13], K -controlled [13], and fully-plastic J -controlled [14] specimens when the driving force (and resistance) for crack growth is constant (i.e., during steady-state crack growth

* Corresponding author.

E-mail address: christopher.muhlstein@mse.gatech.edu (C.L. Muhlstein).

¹ School of Materials Science and Engineering, Georgia Institute of Technology, 771 Ferst Dr NW, Atlanta, GA 30332, USA.

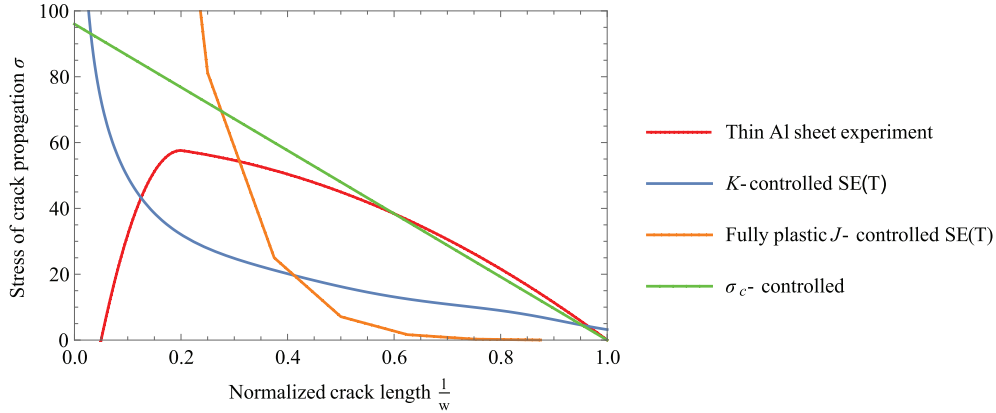


Fig. 1. Schematic of a typical ductile thin sheet's stress-crack length relationship along with curves for steady-state crack growth which is K -controlled [13], fully-yielded plastic J -controlled [14], and σ_c -controlled.

conditions). Fig. 1 also shows the stress vs. crack length behavior of a typical thin ductile metal sheet specimen, which illustrates how σ_c characterizes the portion of the experiment where steady-state crack propagation occurs. This is the power of a fully-yielded plastic crack growth resistance measurement: we can use σ_c in a fully-yielded thin sheet where K and J analysis cannot be easily applied due to extensive plastic deformation (i.e., the plastic deformation is not contained by a computationally convenient zone or field).

Steady-state crack growth is a subject which is often approached analytically [1,3,7,2] but a phenomenon which is rarely measured experimentally under quasistatic loading conditions. The reason such measurements are rare is because of the conditions necessary to make a valid K or J measurement create difficulties in producing steady-state crack growth. Consider a material with crack growth resistance described by a R -curve (i.e., driving force and/or resistance as a function of crack length or crack extension). If a material is capable of quasi-static steady-state crack growth, then it must have some range of crack lengths with a flat R -curve, i.e. $\frac{\delta R}{\delta a} = 0$. Not all materials can necessarily reach a $\frac{\delta R}{\delta a} = 0$ condition. The conditions for measuring valid K or R values also create challenges in experimentally measuring a flat R -curve. Unstable crack growth (and the loss of quasi-static crack growth conditions) occurs when the rate of driving force increase ($\frac{\delta K}{\delta a}$ or $\frac{\delta J}{\delta a}$) exceeds the crack growth resistance $\frac{\delta R}{\delta a}$. In order to measure steady-state crack growth in a material with a K or J -controlled crack, one would have to perform an experiment where $\frac{\delta K}{\delta a} \leq 0$ or $\frac{\delta J}{\delta a} \leq 0$. This requirement eliminates most force-controlled experiments and experiments with significant elastic energy storage (i.e. specimens with small, contained crack tip plastic zones inside a larger elastic strain field). The K and J -controlled stress of crack propagation curves in Fig. 1 show how quickly a specimen under displacement control must decrease stress with increasing crack length (i.e. increase in compliance) in order to exhibit steady-state crack growth characterized by either K or J . On the other hand, a very ductile thin sheet with widespread plastic deformation decreases in stress gradually. While this facilitates experimental measurement, such specimens cannot be characterized using K and pose special challenges for J analysis.

Thin ductile metal sheets give us an opportunity to study quasi-static steady-state tearing, yet they bear little resemblance to conventional analytical descriptions of steady-state tearing [1,3] and defy characterization by conventional K or J analyses. Contrary to analytical models of steady-state crack growth with limited plastic zone size [1,3,7,2], thin ductile metal sheets undergo steady-state crack growth with large-scale yielding [13] which precludes us from using conventional K or J measures of crack growth resistance. We should emphasize that the challenge with using a J -integral based approach in ductile thin sheets is a practical one, not a fundamental limitation of the strain energy release rate crack tip parameter. Established elastic-plastic,

strain hardening process zone descriptions like the HRR field are not applicable to thin, ductile sheets because plasticity in the fracture process zone is so extensive. To use J we must have accurate, experimentally validated three dimensional finite element models that

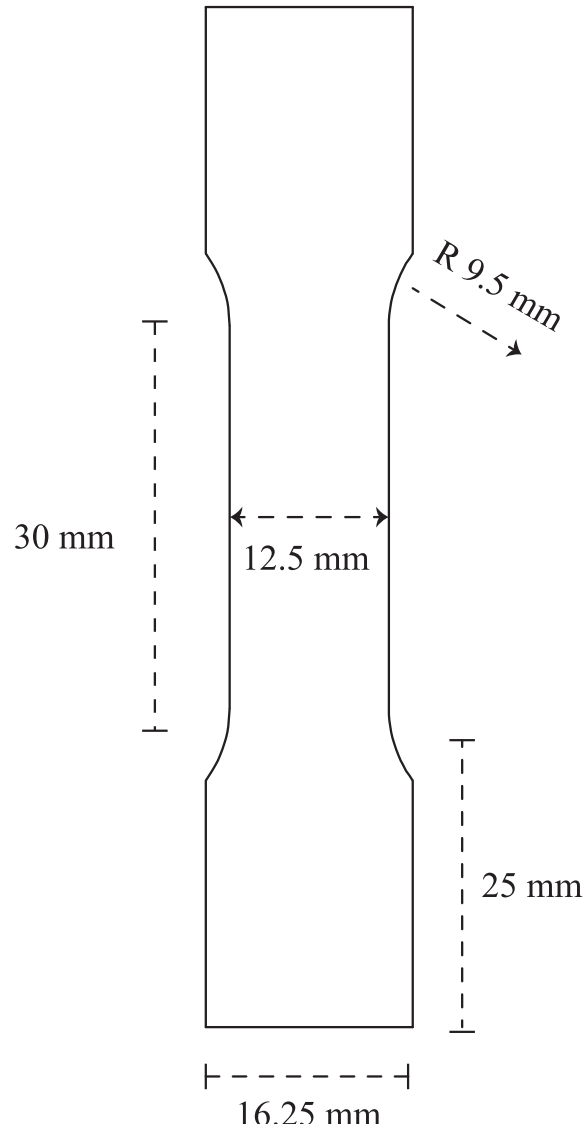


Fig. 2. Specimen dimensions used for all uniaxial testing.

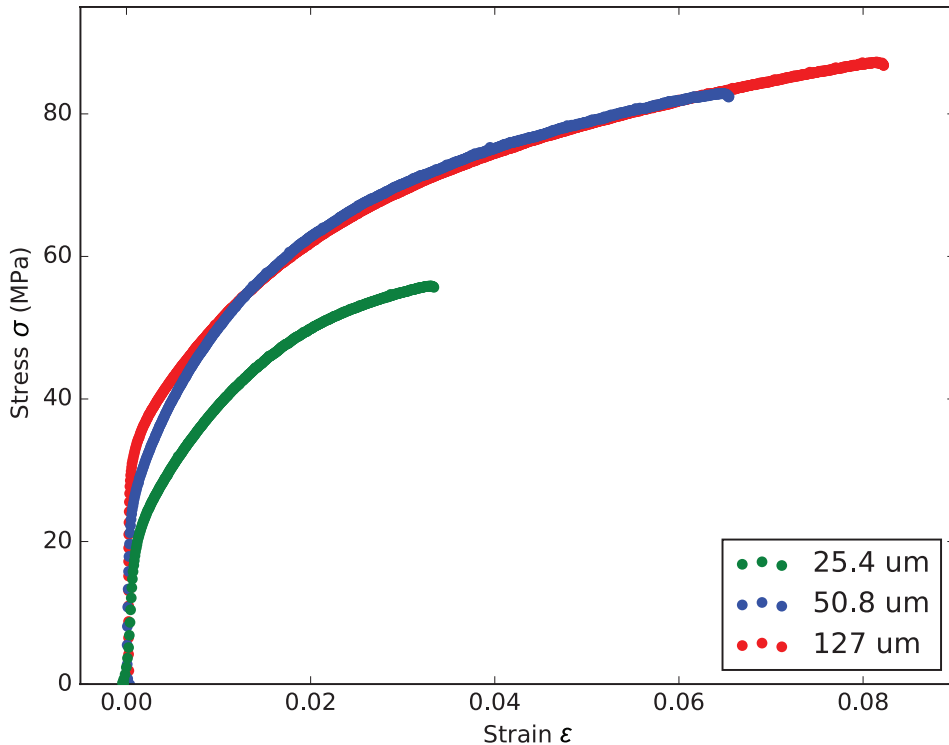


Fig. 3. Uniaxial true stress vs. true strain curves computed from DICT analysis of 25.4 μm , 50.8 μm , and 127 μm thick aluminum tensile specimens. These curves were used to measure the uniaxial tensile properties given in Table 2.

capture the complete deformation history in the vicinity of the crack tip. We are not aware of such models for thin ductile sheets. Alternatively, clever experiment design, such as using double edge notch tensile (DENT) specimens can induce predictable plastic zone scaling as in the case of crack growth resistance with the essential work of fracture concept [11,10]. σ_c has the distinct advantage that it can be measured in a wider variety of thin ductile metal sheets specimens without needing to control or model this plastic zone scaling. In this manuscript, we investigate mode I steady-state crack growth in thin aluminum sheets. We identify the range of crack lengths where steady-state crack growth appears, explore how steady-state crack growth σ_c scales with sheet thickness, and discuss how σ_c relates to sheets' microstructure and uniaxial tensile properties.

2. Materials and methods

2.1. Materials

Tensile specimens (designated “T” elsewhere in this manuscript) were fabricated from 25.4 μm , 50.8 μm , and 127 μm thick commercially pure 1235 aluminum foil stock and cut into dogbone-type geometry based on the ASTM E345 A geometry [15]. The 25.4 μm thick specimens were cut with a 355 nm wavelength machining laser (QuikLaze-50ST2), the 50.8 μm were cut with a Sizzix eClips2 blade cutter, and the 127 μm thick specimens were cut with a Maxiem 1515 waterjet cutter then the edges were smoothed by manually sanding them with 1200 grit SiC abrasive paper. All of the specimens had the same nominal reduced section length (30 mm), reduced section width (12.5 mm), gauge length (20 mm) and fillet radius (9.5 mm) (Fig. 2). A QuikLaze-50ST2 machining laser (20 μm (transverse direction) by 4 μm (tensile direction) exposure area) was used to add 1.0 mm or 2.0 mm notches to the dogbone-type specimens to create single edge notch tension “SE(T)” and middle crack tension “M(T)” fracture mechanics specimens (see Fig. 2).

We cut three strips approximately 1.0 cm by 6.0 cm from each of the

rolls of aluminum sheet for grain size characterization. The as-rolled sheets were only prepared electrochemically (i.e., the films were not thinned or planarized by mechanical polishing). We applied Kapton tape to each specimen so that an area of approximately 1.0 cm \times 6.0 cm was exposed on one end with some exposed metal left at the other for an electrode clamp to attach. Each strip's exposed end was measured with digital calipers and then anodized by immersing it in 2.3% fluoroboric acid solution 1 cm from a parallel 4 cm wide by 6 cm tall cathode cut from the same aluminum stock. The electrolyte was not stirred and at room temperature (about 20 °C). The Kapton tape limited the surface area exposed to the solution as an Agilent E-3612A power supply was used to anodize the specimens with a current density of 155 mA cm $^{-2}$. After 20 s of anodization, we quickly removed the specimens from the electrolyte and gently rinsed them in a warm water bath [16].

We imaged the anodized specimens using an Olympus BX40 optical microscope in bright field mode using the 5× objective and two (U-PO and U-AN360) polarization filters. Twenty random lines were overlaid onto a field of view from each of the three specimens cut from sheets of each of the three thicknesses of aluminum sheet. The number of intercepts between each line and the grain boundaries were manually counted and used to compute a mean lineal intercept (MLI) grain size using the Heyn method ASTM E112 [17]. The mean lineal intercept grain sizes \bar{L} of the sheets were measured as $\bar{L}_{25.4 \mu\text{m}} = 127 \mu\text{m}$, $\bar{L}_{50.8 \mu\text{m}} = 120 \mu\text{m}$, and $\bar{L}_{127 \mu\text{m}} = 177 \mu\text{m}$.

We characterized the texture of each sheet using a PANalytical XPert MRD Pro diffractometer in parallel beam geometry with Cu- K_{α} radiation through a sealed Cu tube (45 kV/40 mA) and a graphite monochromator, a polycapillary X-ray lens (1 mm \times 1 mm), an Eulerian cradle and a proportional counter. We used glancing angle measurements to characterize the texture to different depths into the aluminum sheets. For each sheet, the texture was characterized at approximately half of the sheet thickness and the entirety of the sheet thickness in order to determine whether there was any textural asymmetry between the different sides of the sheets. An open source MATLAB program

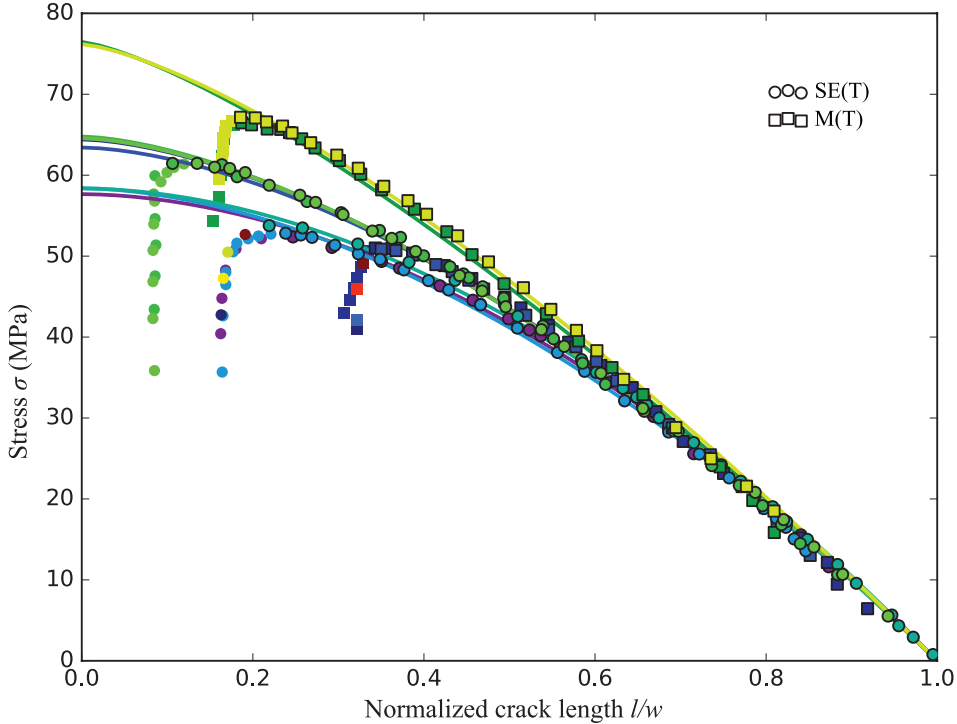


Fig. 4. Crack propagation stress analysis of $25.4\text{ }\mu\text{m}$ specimens including power law fits of the data (Eq. (3)) used to determine convergence. Individual experiments are differentiated by marker and curve fit color, and black marker borders indicate the propagation portion of the experiment used with Eq. (3) to determine convergence of the data. (For interpretation of the references to color in this figure legend, the reader is referred to the web version of this article.)

MTEX v.4.3 was used to analyze the texture data obtained and generate pole figures.

2.2. Specimen preparation and experimental methods

A total of 34 tearing and 11 uniaxial tensile tests were conducted. All specimens were placed onto paper backings before being fixed in the load frame grips which helped prevent wrinkling and misalignment as they were placed in the test frame grips. The specimen's grip sections were glued to the paper backing, while the fillets and reduced section

were laid flat against the paper but otherwise free. The specimens were then placed in the load frame's wedge grips which were then tightened. Once the specimens were secured in the grips, the portion of the paper backing behind the reduced section was removed.

All specimens were tested with an Instron 5848 (Instron, Norwood, MA) load frame equipped with a magnetic linear encoder with a 20 nm resolution (Heidenhain, Schaumburg, IL) placed on a bench top vibration isolated platform (BM-4, Minus K Technology, Inglewood, CA). Please note that this is a high precision, low force, closed loop load frame that does not have the backlash other control issues that are often

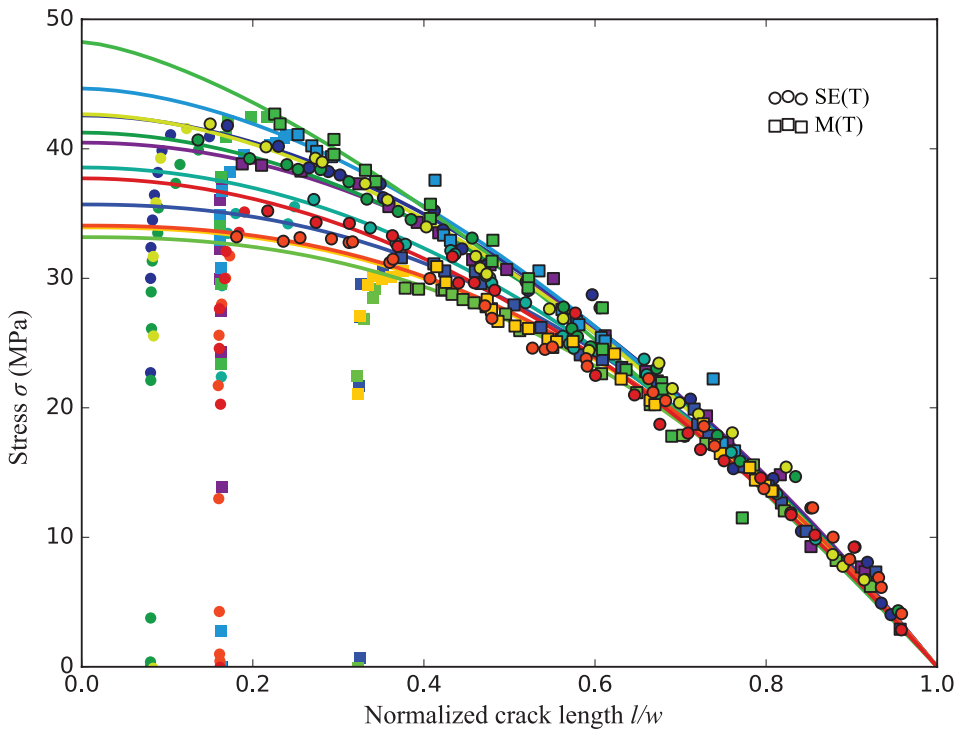


Fig. 5. Crack propagation stress analysis of $50.8\text{ }\mu\text{m}$ specimens including power law fits of the data (Eq. (3)) used to determine convergence. Individual experiments are differentiated by marker and curve fit color, and black marker borders indicate the propagation portion of the experiment used with Eq. (3) to determine convergence of the data. (For interpretation of the references to color in this figure legend, the reader is referred to the web version of this article.)

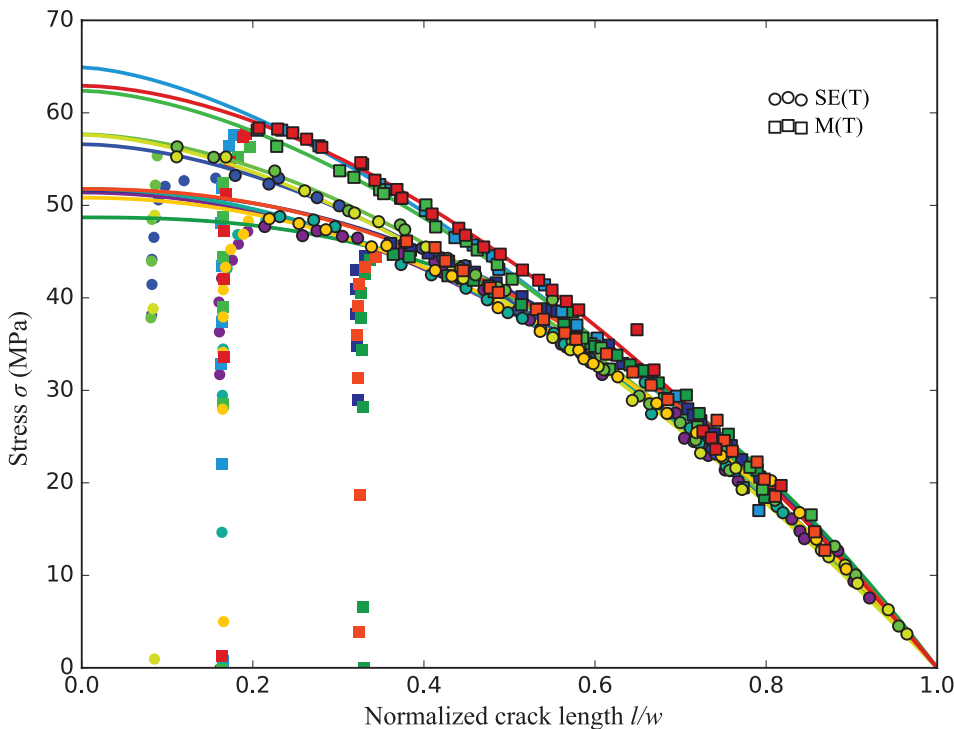


Fig. 6. Crack propagation stress analysis of 127 μm specimens including power law fits of the data (Eq. (3)) used to determine convergence. Individual experiments are differentiated by marker and curve fit color, and black marker borders indicate the propagation portion of the experiment used with Eq. (3) to determine convergence of the data. (For interpretation of the references to color in this figure legend, the reader is referred to the web version of this article.)

associated with using high capacity load frames at low loads. All specimens were held in the low force testing frame with wedge grips. A 100 N Instron 2530-427 static load cell was used for the 25.4 μm and 50.8 μm thick specimens and an Instron 1500ASK 1000 N static load cell was used for the 127 μm thick specimens. The associated uncertainty in stress was 0.1% of the calculated value. Experiments were controlled by a custom-built program written in NI Labview 7.1 using a GPIB interface to control the load frame and record force and displacement data. All tests were performed in displacement control with a crosshead displacement rate of 0.01 mm s^{-1} for the 25.4 μm and 50.8 μm thick specimens and 0.025 mm s^{-1} for the 127 μm thick specimens with an estimated local strain uncertainty of 0.4%.

A 24 megapixel (6000×4000) Nikon D3300 DSLR camera fitted with a Nikon macro lens was used to capture images before and during experiments. The specimens were illuminated with a 50.8 mm Dolan-Jenner FLD light diffuser connected to a Dolan-Jenner Fiber-Lite light source, and the camera was positioned such that it viewed the specimens *through* the light diffuser. Thus, images were captured with an illumination condition analogous to bright field microscopy. The SE(T) and M(T) specimens were tested with a second fiber optic light source placed behind the specimens which facilitated optical crack growth measurement by illuminating the growing crack. The camera settings were ISO 100, aperture f/13, and shutter 1/320 s. The camera was triggered using an Arduino Mega microcontroller with custom firmware which triggered the camera at a rate of 1 Hz using a connector wired from the Arduino to the camera's accessory port. The camera trigger microcontroller was synchronized to the experiment start with a TTL signal wired directly to the camera from the Instron load frame controller. The force, displacement, and image capture data were synchronized to within 1 μs . The images captured during the experiment were then used to measure the crack length of SE(T) and M(T) experiments with ($6 \mu\text{m}$) spatial resolution vs. a minimum notch size of 1.0 mm indicating an estimated crack measurement uncertainty of 0.6%. The experiments were stopped when the cracks either reached the far edge of the specimens or a secondary crack initiated from the back edge. Representative fracture surfaces and fracture profiles were imaged using a Hitachi TM3030 bench-top scanning electron microscope (SEM) in "COMPO" backscatter imaging mode.

In addition to crack growth experiments, we also performed uniaxial tensile experiments on straight gage specimens without notches. The specimens were speckled with a light dusting of acrylic paint to give the surface additional contrast for digital image correlation and tracking (DICT). These specimens were then tested in tension under the same conditions as the other experiments, except with a slower cross-head displacement of 0.0025 mm s^{-1} in order to allow for capture of a larger number of images. (The force-displacement curves were compared to the faster experiments to verify that strain rate effects did not significantly alter the results.) A regular grid of points was defined in the first image and then tracked through the image sequence using a Python (Anaconda 2.7) implementation of the OpenCV sparse optical flow feature tracking algorithm calcOpticalFlowPyrLK. Any features that the algorithm failed to find or could not be tracked back to within 2 pixels of their location in the previous image in the sequence were discarded. We then applied a linear interpolation scheme to a Voronoi triangulation of the points and their displacements, resulting in a continuous displacement field. We then took the gradient of the displacement field to compute a strain field, from which we computed an average strain we used in uniaxial stress-strain curves. Those stress-strain curves (see Fig. 3) were used to compute the elastic moduli, 0.2% offset yield strengths, and Ramberg-Osgood parameters (see Table 2). The average ultimate engineering tensile strengths σ_{us} were 53 MPa ($B = 25.4 \mu\text{m}$, 3 specimens), 75 MPa ($B = 50.8 \mu\text{m}$, 3 specimens), and 81 MPa ($B = 127 \mu\text{m}$, 3 specimens).

2.3. Crack propagation stress

The crack propagation stress analysis to extract the steady-state crack growth resistance uses a plot of nominal stress $\sigma = \frac{P}{B \times w}$ as a function of normalized crack length $\sigma(\frac{l}{w})$, where P is the applied force, B is the specimen thickness, and w is the specimen width. The definition of crack length, though, is a subtle but important distinction from other fracture toughness conventions. For this study, we will use the total crack length l rather than the conventional crack length per crack tip a usually used in fracture mechanics. Thus for our SE(T) and M(T) configurations the crack lengths are $l_{SE(T)} = a$ and $l_{M(T)} = 2a$. The choice to

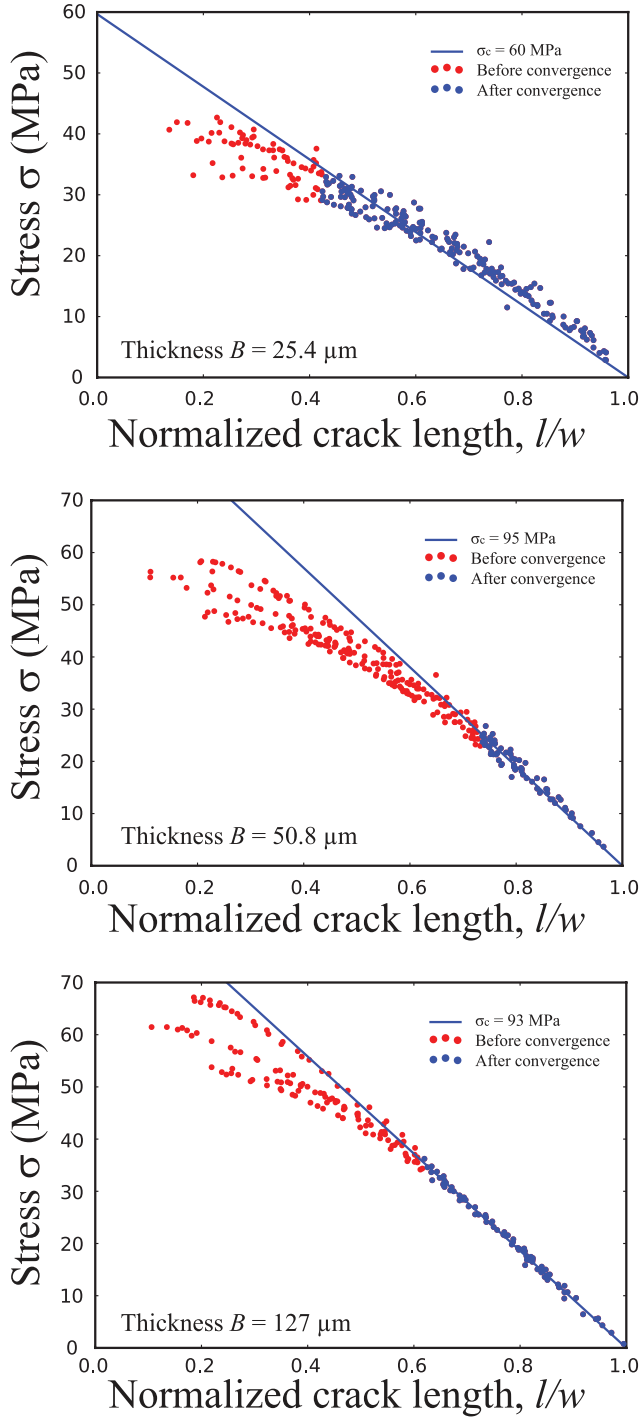


Fig. 7. Nominal stress vs. normalized crack length plots showing the combined datasets for each specimen thickness, the demarcation between data points before and after convergence of the experiments, and the linear fit to the converged data points.

Table 1

Measured values of steady-state crack growth resistance σ_c and the standard deviation of the converged data subset (confidence level of $p = 0.01$) from the line corresponding to σ_c .

Thickness B (μm)	Converged σ_c (MPa)	Standard deviation (MPa)
25.4	60	2.3
50.8	95	1.3
127	93	0.66

use the normalized crack length $\frac{l}{w} = \frac{a_{SE(T)}}{w} = \frac{2a_{M(T)}}{w}$ resulted in a convergence in the crack propagation curves of the different specimens. As detailed in [13], the convergence of different specimens' crack growth curves defines the onset of steady-state crack growth and similitude. Once steady-state has been reached, the nominal stress decreases linearly with normalized total crack length and a characteristic steady state stress, σ_c , is defined.

2.4. ANOVA of residuals for detecting convergence

Nominal stress (σ) vs. normalized crack length ($\frac{l}{w}$) plots showed that SE(T) and M(T) specimens with different starting notch lengths converge after a certain amount of crack growth. We formulated a quantitative measure of convergence by applying analysis of variance (ANOVA) to the residuals of nonlinear least squares fits of a power law function to the propagation $\sigma(\frac{l}{w})$ data points (i.e. the data points *after* the maximum stress was reached). The details of the algorithms and their (open source) implementation are detailed in Appendix A.

3. Results and discussion

Though ductile thin metal sheets offer an opportunity to characterize quasi-static mode I steady-state crack propagation, it is important to identify the onset of steady-state crack growth. Figs. 4–6 show the stress of crack propagation analyses for the $25.4 \mu\text{m}$, $50.8 \mu\text{m}$, and $127 \mu\text{m}$ thick specimens, respectively. In all three cases, the different notch lengths in SE(T) and M(T) specimens initiated crack growth at different stress levels and crack lengths, but their crack growth curves converged with one another after some crack propagation. In our previous publication [13], we fit the entire crack propagation curve to a line corresponding to a single value of σ_c . For this study, we used a more rigorous, iterative ANOVA of residuals analysis to identify the crack lengths where both the SE(T) and M(T) specimens' cracks were propagating at the same nominal stress values. Then we fitted this subset of the crack propagation curve to a constant σ_c line (Eq. (1) and Fig. 7).

$$\sigma = \sigma_c \times \left(1 - \frac{l}{w}\right) \quad (1)$$

Eq. (1) was rearranged to show that σ_c was the effective stress in the net section (i.e. uncracked ligament).

$$\begin{aligned} \sigma_c &= \sigma \times \left(1 - \frac{l}{w}\right)^{-1} \\ \sigma_c &= \frac{P}{B \times w} \times \frac{w}{w-l} \\ \sigma_c &= \frac{P}{B \times (w-l)} = \frac{P}{B \times (w-l)} \end{aligned} \quad (2)$$

The characteristic stress (parameter) of our analysis, σ_c , was a measure of the steady-state crack growth resistance of the thin aluminum sheets. The steady-state crack growth resistance, σ_c , for each of the thicknesses tested was 60 MPa, 95 MPa, and 93 MPa for the $25.4 \mu\text{m}$, $50.8 \mu\text{m}$, and $127 \mu\text{m}$ thick specimens, respectively (Table 1). Though σ_c -controlled crack growth occurred in a fully-yielded specimen rather than a contained plastic zone as described by analytical models of J -controlled steady-state crack propagation [2], in both cases the steady-state was approached asymptotically as the crack advanced. Our ANOVA of residuals technique detected when an experiment had converged to σ_c -controlled growth. The convergence of SE(T) and M(T) specimens showed that even specimens with different initial conditions eventually approached steady-state crack propagation with the same σ_c (Table 1). It is important to note that the nominal stress as a function of the normalized crack size did not uniquely characterize the initiation and transition stages of the tearing process. However, once steady-state conditions were reached σ_c was predictive because the driving force scaled linearly with normalized crack length. While the steady-state

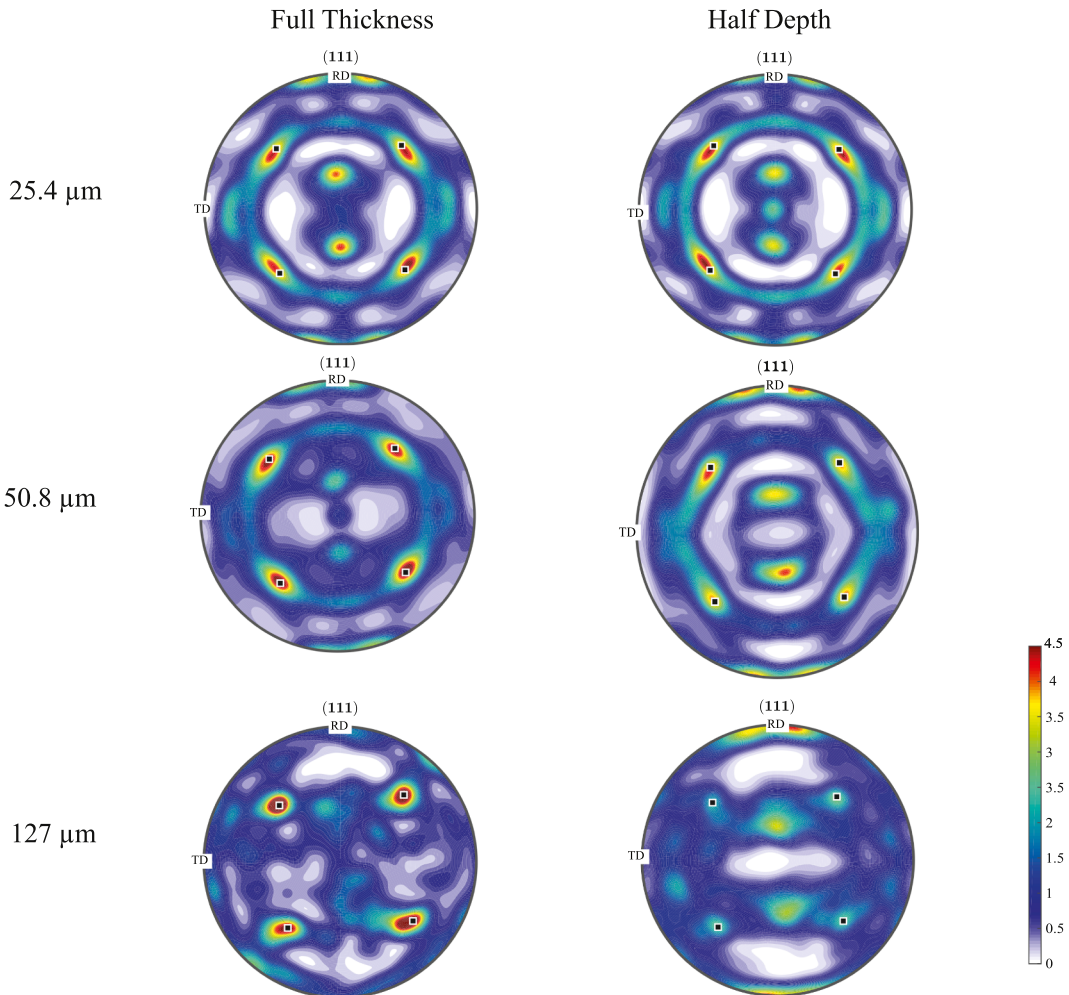


Fig. 8. X-ray diffraction (111) pole figures for each thickness. We used glancing angle XRD to sample the microstructure through the whole thickness B as well as half-way through the thickness. Though the peak count varied somewhat between specimens, the location and orientation of the peaks within the pole figures was the same for all sheet thicknesses, and the similarity of the full-thickness and half-thickness scans indicates no difference in the texture of the different sides of the rolled and annealed 1235 aluminum sheets.

crack growth resistance, σ_c , captured the scaling of the driving force for crack advance, it was not a true crack tip parameter. As a result, additional developments will be required to relate σ_c to the crack tip stress field.

Though σ_c -controlled and J -controlled steady-state crack growth are conceptually similar in that in both cases the steady-state is approached asymptotically, there are some major differences in the different parameters' relationship to crack extension and crack length. A J -controlled specimen approaches steady-state crack propagation after a certain amount of crack extension, and thus the crack's starting place is an important reference point. In such cases the crack growth resistance is commonly expressed with a $J(\Delta a)$ crack extension J - R curve. On the other hand, σ_c is a parameter which depends primarily on the uncracked ligament length ($w - l$) rather than the absolute length of the crack (a or l) itself. This is part of why σ_c -controlled growth was easiest to identify on a stress vs. normalized crack length plot (Fig. 1). Our previous publication featured a discussion of how σ_c -controlled crack growth manifested in a analysis [13]. In our thin aluminum sheets, steady-state crack growth did not progress inside of an invariant, well-contained plastic zone as described by J -based analyses, but inside a fully-yielded uncracked ligament. Though the extensive plasticity in the specimens precluded a K or J -based analysis of their steady-state crack growth resistance, σ_c was a useful tool for exploring how steady-state crack growth was affected by specimen thickness and microstructure.

The variability within the different sheets' converged crack propagation curves was affected by an interaction between specimen microstructure and sheet thickness (Fig. 7). The 25.4 μm thick specimens' data retained the most curvature in the converged data subset while the 127 μm thick specimens' data appeared to match the linear fit most closely. This qualitative observation was supported by the standard deviation of the residuals of the linear fits of the truncated data sets, which were 2.3 MPa, 1.3 MPa, and 0.7 MPa for the 25.4 μm , 50.8 μm , and 127 μm thick specimens, respectively (Table 1). The reason for the thinnest specimens' convergence at a relatively low normalized crack length and retention of curvature was the greater variability within the individual experiments using the 25.4 μm thick sheets. Since the ANOVA of residuals analysis was a comparison between the variation within individual experiments to the variation between the experiments, the greater spread of data within the individual 25.4 μm experiments reduced the amount of variation between the experiments necessary to satisfy the null hypothesis for the confidence level used. This variation in the stress needed to propagate the crack was consistent with literature observations that as the dimensions of specimens decreased relative to their grain size, the variability in their mechanical properties increased [18]. The mean lineal intercept grain size \bar{L} for each sheet was greater than the sheet thickness: $\bar{L}_{25.4\ \mu\text{m}} = 127\ \mu\text{m}$, $\bar{L}_{50.8\ \mu\text{m}} = 120\ \mu\text{m}$, and $\bar{L}_{127\ \mu\text{m}} = 177\ \mu\text{m}$. The textures of the texture of the three thicknesses of sheet were very similar

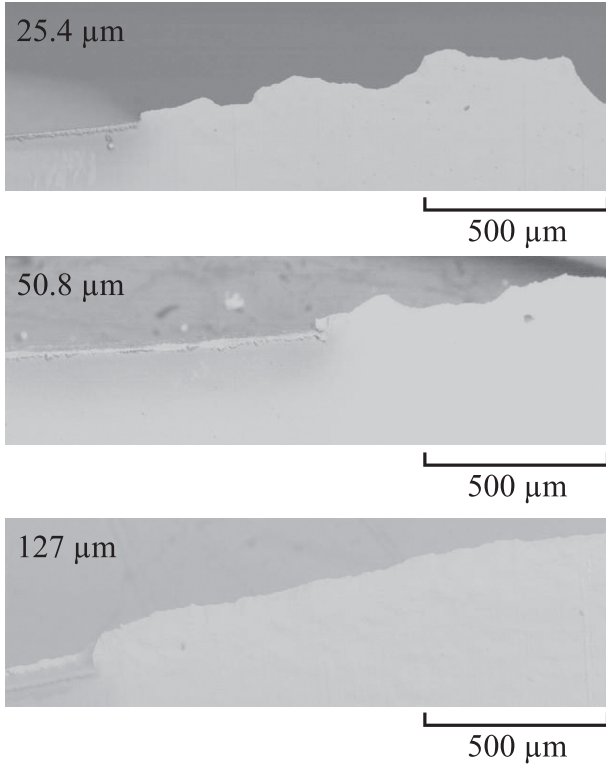


Fig. 9. Fracture profiles of 25.4 μm , 50.8 μm , and 127 μm thick M(T) specimens showing the laser-cut notch (at left) the transition to ductile tearing, and the ductile tearing fracture surface.

(Fig. 8). The 25.4 μm and 50.8 μm sheets make an interesting point of comparison since they had such similar grain sizes. The thinner 25.4 μm specimens had a relatively small near-crack necking region which encompassed fewer grains, which in turn resulted in greater variability in crack propagation compared to the 50 μm specimen with a slightly smaller grain size.

The crack paths and fracture surfaces of both M(T) and SE(T) specimens of all sheet thicknesses (Figs. 9 and 10) showed that the crack growth mechanism was reduction of the sheet thickness (transverse necking) at the crack tip before separation with some small voids appearing at the center of the resulting ridge. The lack of variation in the fracture surfaces suggested that while the driving force for crack growth may have evolved before finally converging to σ_c and steady-state crack propagation, the transition did not leave obvious visible signs and the mechanism of crack advance itself did not change. The fracture profiles of the different thicknesses were all similar to one another, but the side-view of the specimens revealed some differences in the crack paths (Fig. 9). The 25.4 μm thick sheets showed a (qualitatively) tortuous crack path compared to the relatively straight path followed by the crack in the 127 μm thick specimen, with the 50.8 μm specimen as an intermediate case between the two. There was no evidence of a dramatic change in crack path or mechanism of crack advance as the specimens approached steady-state crack growth. The decrease in crack path tortuosity with increasing thickness fits in with our prior discussion of the interaction between thickness, grain size, and variation in the crack propagation curves.

The properties we measured with DICT help explain the relatively low steady-state crack growth resistance of the 25.4 μm thick sheets compared to the other specimens. Specifically, the in-plane contraction ratio η_w scaled with thickness, which indicated thickness-dependent anisotropy of plastic flow. The contraction ratio η_w was the negative ratio of an increment in transverse strain to the corresponding increment in axial strain, i.e. $\eta_w = -\frac{d \epsilon_w}{d \epsilon_{ax}}$ where ϵ_{ax} was the strain in the

direction of the applied force and ϵ_w was the strain in the width direction (i.e. the direction perpendicular to the loading axis and in the plane of the sheet). All of the tensile specimens converged to a constant value of η_w for post-yield strains. Bulk metal have isotropic contraction ratios $\eta = \nu$ during elastic deformation (ν is Poisson's ratio) which approach ideal isotropic, isochoric behavior during plastic deformation: i.e. constant-volume and $\eta = 0.5$ [19]. We measured values of η which were constant between yield and specimen rupture, but *not* consistent with isotropic transverse strains $\eta = 0.5$ (Table 2). By assuming constant volume, we can compute the through-thickness contraction ratio $\eta_B = 1 - \eta_w$. Thus, the 25.4 μm sheets contracted more than twice as much perpendicular to the sheet surface $\eta_B = 0.68$ compared to contraction within the plane of the sheet $\eta_w = 0.32$ for a given increment in axial strain. The in-sheet contraction $\eta_B = 0.32$ was nearly the same as for elastic deformation $\nu = 0.33$ [20], even though η_B was measured post-yield. The thicker sheets also favored through-thickness contraction over in-plane contraction, but approached the isotropic isochoric contraction ratio $\eta_B = \eta_w = 0.5$ with increasing thickness. Steady-state crack growth was a transverse necking process, so we propose that the greater propensity for through-thickness contraction of the 25.4 μm thick specimens ($\eta_B = 0.68$) relative to the 50.8 μm thick specimens ($\eta_B = 0.63$) was a contributing factor to the lower steady-state crack growth resistance we measured in the 25.4 μm thick specimens ($\sigma_{c,25.4 \mu\text{m}} = 60 \text{ MPa}$ vs. $\sigma_{c,50.8 \mu\text{m}} = 95 \text{ MPa}$).

The properties of thin ductile metal sheets must be controlled by a combination of microstructure and specimen dimensions. So far we have attributed differences in steady-state crack growth resistance, σ_c , between the 25.4 μm and 50.8 μm primarily to thickness. We can make this comparison with some confidence because the two sheet thicknesses were the same 1235 alloy, were annealed, had nominally the same texture (Fig. 8), and had similar in-plane mean lineal intercept grain sizes ($L_{25.4 \mu\text{m}} = 127 \mu\text{m}$ and $L_{50.8 \mu\text{m}} = 120 \mu\text{m}$) which were significantly larger than the sheet thicknesses. Thus, the 25.4 μm and 50.8 μm thick sheets had nearly the same microstructure and differed primarily in thickness. On the other hand, the 127 μm thick sheets had a MLI grain size which was larger than the other two and closer to the sheet thickness ($L_{127 \mu\text{m}} = 177 \mu\text{m}$), which made differentiation between thickness effects and microstructural effects difficult. However we were still able to look at what properties did and did not follow a clear trend with thickness to infer the relative importance of sheet thickness and microstructure to the material properties.

The nominal net section stress of steady-state crack propagation σ_c (Table 1) exceeded the yield stress, σ_y , shown in Table 2, indicating that for all specimens σ_c -controlled steady-state crack propagation occurred in a fully-yielded ligament ahead of the crack tip. The yield strength increased with increasing thickness for all three thicknesses tested (Table 2). The thickest sheet also had the largest mean lineal intercept grain size ($L_{127 \mu\text{m}} = 177 \mu\text{m}$), which ran contrary to both Hall-Petch strengthening by grain boundaries and the observations of [21,22] of much thinner ($<1.0 \mu\text{m}$) FCC metal films where decreased grain size and/or thickness correlated with increased yield strength. The scaling of the yield strength and contraction ratio with thickness both indicate that thinner sheets promoted through-thickness contraction (necking). Easier through-thickness contraction due to thickness explained the decrease in steady-state crack growth resistances between the 50.8 μm and 25.4 μm thick sheets which had very similar microstructures. However, we did not observe a similar scaling between the 50.8 μm and 127 μm thick sheets, which showed that the microstructure still influenced σ_c significantly, especially when the in-plane grain size approached the sheet thickness. The 25.4 μm thick specimens had low apparent elastic modulus $E_{25.4 \mu\text{m}} = 23 \text{ GPa}$ compared to the thicker specimens $E_{50.8 \mu\text{m}} = E_{127 \mu\text{m}} = 61 \text{ GPa}$ (Table 1) and the ASM Handbook value for annealed pure aluminum $E = 69 \text{ GPa}$ [20]. Elastic moduli much lower than the expected bulk, polycrystalline aggregate (or texture corrected) values have been routinely reported in very thin sheets, foils, and films. Originally discussed by Mott [23] and Friedel [24],

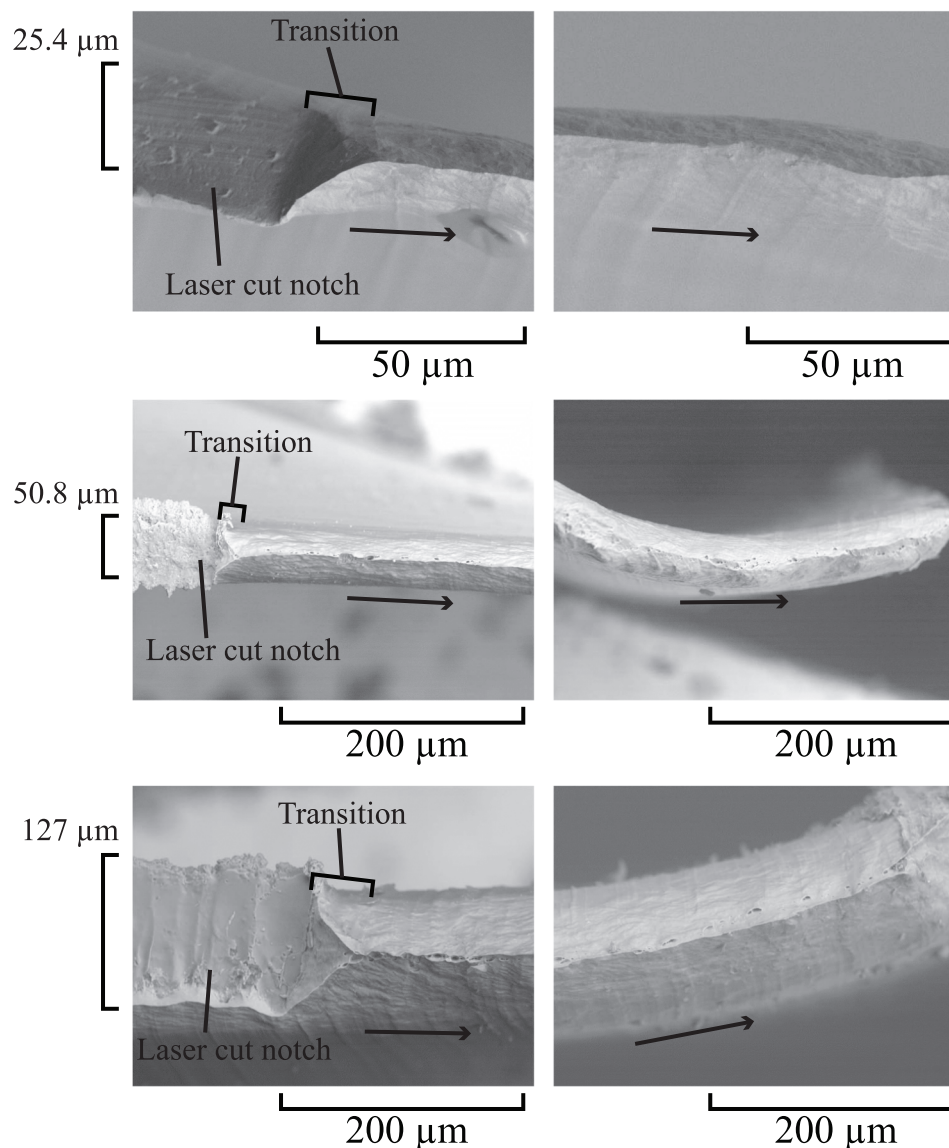


Fig. 10. Representative fracture surfaces of each thickness of aluminum sheets used in this study including both the starting notch and a segment near the back edge. Arrows indicate direction of crack growth.

“low” elastic moduli have been routinely discussed in the mechanical spectroscopy and sheet metal forming literature and have been attributed to the elastic motion of pinned dislocations that interact with the Pierls stress of the lattice and other defects (especially point defects). A summary of the modern literature is detailed in the handbook by Blanter et al. [25]. The mechanical spectroscopy literature on pure and alloyed metals, including Al, on this topic is extensive (a summary for Al can be found in Section 4.3 of [25]). In short, dislocation-point defect interactions can be a source of significant energy dissipation in metals at room temperature. These strains scale linearly with stress and manifest themselves as low elastic moduli during tensile tests. Depending on the defect structure and material form, the apparent moduli

have been 10s of percent lower than the expected polycrystalline aggregate and texture-corrected elastic modulus values (for low modulus thin foil/film Al data see [26–34]). The low modulus in our 25.4 μm thick sheet was experimentally valid based on our calibration procedures, analyses, and the existing literature. It is useful to note that slight errors in elastic modulus do not influence our conclusion that through-thickness contraction became easier with decreasing sheet thickness.

Thin ductile metal sheets present an opportunity to characterize how mode I steady-state crack growth relates to specimen thickness and microstructure. However, crack growth in these sheets challenges conventional fracture mechanics approaches such as K and J because these crack tip parameters require relatively small crack tip plastic zone

Table 2

Uniaxial tensile properties of thin 1235 aluminum sheets from DICT analysis. Yield stress σ_y and yield strain ϵ_y were computed with the 0.2% offset method.

Thickness B (μm)	Elastic modulus E (GPa)	Yield strength σ_y (MPa)	Yield strain ϵ_y	In-plane contraction ratio η_w	Ultimate tensile strength σ_{uts} (MPa)
25.4	23	27	0.0032	0.32	53
50.8	61	33	0.0026	0.37	75
127	61	38	0.0026	0.42	81

sizes. In contrast, the thin aluminum sheets used in this study exhibited steady-state crack propagation characterized by the fully-plastic, steady state crack growth resistance parameter, σ_c . Unlike the linear-elastic K and elastic-plastic J parameters, σ_c depends on the uncracked ligament length ($w - l$) rather than on the crack length l (or a) or crack extension Δa . In principle a σ_c -controlled crack could be of any length, and the mode I steady-state tearing resistance would still depend solely on how much uncracked specimen remained. This does not mean that the crack is unimportant though, or even that the uncracked ligament has a uniform stress equal to σ_c all of the way across. In all of our experiments, fracture still proceeded from the crack tip, not from any other portion of the uncracked ligament, and significant crack propagation was necessary before the experiments converged to σ_c -controlled steady-state crack propagation.

4. Conclusions

Steady-state tearing is typically associated with constrained crack tips and limited plastic zones due to constraint and specimen size [1,3], specialized specimen design [11,35], and steady-state creep crack growth [7,9]. However, the requirement of a limited plastic zone size is

more a prerequisite for conventional fracture mechanics analyses of crack growth resistance than a requirement for steady-state crack propagation. Our crack propagation stress analysis of thin ductile metal sheets revealed a range of crack lengths where the steady-state crack growth resistance is characterized by a characteristic stress, σ_c . The steady-state crack growth resistance is tied to the length of the uncracked ligament ahead of the crack tip ($w - l$) rather than the crack length. Both SE(T) and M(T) specimens ultimately converged to a single driving force, σ_c , after a transitional stage of crack growth. Thus we have demonstrated that steady-state crack growth conditions develop during crack propagation in thin, ductile metal sheets.

Acknowledgments

This material is based upon work supported by the National Science Foundation under Grant No. 1609817. Any opinions, findings, and conclusions or recommendations expressed in this material are those of the authors and do not necessarily reflect the views of the National Science Foundation. The authors gratefully acknowledge the additional support of the Georgia Institute of Technology.

Appendix A

Here we detail the general features of the algorithm and the specific open source statistics packages that were used. All of this analysis was performed using the open source Anaconda Python 2.7 (64-bit). First, we used the `optimize.curve_fit` function from the open source `numpy` Python package to fit the propagation data of the experiments to be compared to the power law given in Eq. (3).

$$\hat{\sigma} = c \times \left(1 - \left(\frac{l}{w}\right)^m\right) \quad (3)$$

It is important to note that we chose the form of Eq. (3) because it represents the data well and is thus useful for comparing the different experiments to one another, not because it has any explicit physical meaning that we have identified. In this publication, we denote experimentally-measured stresses as σ and stress values computed from a fit as $\hat{\sigma}$. Additionally w is the specimen width, c is a fitting parameter with stress units, and m is a unitless fitting parameter. The analysis involved fits to the individual experiments $\hat{\sigma}_i$ (i is the index of an individual experiment) as well as a fit of all of the experiments combined together $\hat{\sigma}_I$ (index I indicates all of the experiments combined). From there we computed the residuals of the fits.

$$\begin{aligned} r_{i\kappa} &= \sigma_{i\kappa} - \hat{\sigma}_i \left(\left(\frac{l}{w} \right)_{i\kappa} \right) \\ r_{I\kappa} &= \sigma_{i\kappa} - \hat{\sigma}_I \left(\left(\frac{l}{w} \right)_{i\kappa} \right) \end{aligned} \quad (4)$$

The measured data points are given as $\sigma_{i\kappa}$ and $\left(\frac{l}{w} \right)_{i\kappa}$, which is the measurement κ taken from experiment i . (Note that the subscript indices are meant to indicate individual experimental measurements of stress and crack length and simplify the ANOVA sum of squares notation. Do not confuse the indices with the similar notation of stress tensors.) The fits $\hat{\sigma}_i$ share the subscript of the experiment from which they were computed i . The fit of all the experiments combined I is $\hat{\sigma}_I$. Thus for every data point κ from each experiment i , we computed both a residual relative to individual experiment's fit $r_{i\kappa}$ and a residual relative to the fit of all of the combined data $r_{I\kappa}$. The remainder of the analysis is a typical ANOVA of the residuals. First, the sum of squares of residuals within experiments $SoSW$ is:

$$\begin{aligned} SoSW &= \sum_{i=1}^I \sum_{\kappa=1}^{K_i} (r_{i\kappa})^2 \\ df_{SoSW} &= \left(\sum_{i=1}^I K_i \right) - I = n - I \end{aligned} \quad (5)$$

The summation encompasses the total number of experiments I we compared and the total number of measurements within each individual experiment K_i . The degrees of freedom for $SoSW$ is df_{SoSW} , which incorporates the grand total n of measurements from all of the experiments combined I . Rather than directly computing the sum of squares of residuals between experiments, we computed the total sum of squares of residuals $SoST$.

$$SoST = \sum_{i=1}^I \sum_{\kappa=1}^{K_i} (r_{I\kappa})^2 \quad (6)$$

And then computed the desired sum of squares of residuals between experiments $SoSB$.

$$\begin{aligned} SoST &= SoSW + SoSB \\ SoSB &= SoST - SoSW \\ df_{SoSB} &= I - 1 \end{aligned}$$
(7)

The final step of the ANOVA is computation of the mean sums of squares and a F value computation, which in conjunction with the degrees of freedom of the respective sums of squares (df_{SoSW} and df_{SoSB}) was used to compute p-values using the open source SciPy “stats” module: `scipy.stats.f.sf(F, dfSoSW, dfSoSB)`.

$$F = \frac{SoSB/df_{SoSB}}{SoSW/df_{SoSW}}$$
(8)

Our ANOVA of residuals gave us a metric of the strength of the hypothesis that the individual experiments resulted in the same data. We used the ANOVA of residuals as a quantitative test of convergence of the different experimental data sets. We iteratively removed the shortest normalized crack length datapoint ($(\frac{l}{w}, \sigma_{lx})$) from consideration, then the next shortest normalized crack length data point was excluded, and so on while recalculating the entire ANOVA of residuals getting a new F test and p-value each time. Once the p-value exceeded a confidence level of 0.01, we considered the data to have converged.

Appendix B. Supplementary material

Data associated with this article can be found in the SMARTech repository at <http://hdl.handle.net/1853/60642>.

References

- [1] J. Amazigo, J. Hutchinson, Crack-tip fields in steady crack-growth with linear strain-hardening, *J. Mech. Phys. Solids* 25 (2) (1977) 81–97, [https://doi.org/10.1016/0022-5096\(77\)90005-9](https://doi.org/10.1016/0022-5096(77)90005-9).
- [2] B. Cotterell, A. Atkins, A review of the J and I integrals and their implications for crack growth resistance and toughness in ductile fracture, *Int. J. Fract.* 81 (4) (1996) 357–372, <https://doi.org/10.1007/BF00012428>.
- [3] A. Pineau, A. Benzerqa, T. Pardoen, Failure of metals i: Brittle and ductile fracture, *Acta Mater.* 107 (2016) 424–483, <https://doi.org/10.1016/j.actamat.2015.12.034>.
- [4] X.-K. Zhu, J.A. Joyce, Review of fracture toughness (G, K, J, CTOD, CTOA) testing and standardization, *Eng. Fract. Mech.* 85 (2012) 1–46, <https://doi.org/10.1016/j.engfracmech.2012.02.001>.
- [5] A. Rosakis, O. Samudrala, D. Coker, Cracks faster than the shear wave speed, *Science* 284 (5418) (1999) 1337–1340, <https://doi.org/10.1126/science.284.5418.1337>.
- [6] C. Hui, H. Riedel, The asymptotic stress and strain field near the tip of a growing crack under creep conditions, *Int. J. Fract.* 17 (4) (1981) 409–425, <https://doi.org/10.1007/BF00036192>.
- [7] C. Hui, K. Wu, The mechanics of a constantly growing crack in an elastic power-law creeping material, *Int. J. Fract.* 31 (1) (1986) 3–16, [https://doi.org/10.1016/0020-7683\(86\)90010-7](https://doi.org/10.1016/0020-7683(86)90010-7).
- [8] C. Hui, The mechanics of self-similar crack-growth in an elastic power-law creeping material, *Int. J. Solids Struct.* 22 (4) (1986) 357–372, <https://doi.org/10.1007/BF00033925>.
- [9] H. Riedel, Creep deformation at crack tips in elastic-viscoplastic solids, *J. Mech. Phys. Solids* 29 (1) (1981) 35–49, [https://doi.org/10.1016/0022-5096\(81\)90014-4](https://doi.org/10.1016/0022-5096(81)90014-4).
- [10] B. Cotterell, J. Reddel, Essential work of plane stress ductile fracture, *Int. J. Fract.* 13 (3) (1977) 267–277, <https://doi.org/10.1007/BF00040143>.
- [11] B. Cotterell, T. Pardoen, A. Atkins, Measuring toughness and the cohesive stress-displacement relationship by the essential work of fracture concept, *Eng. Fract. Mech.* 72 (6) (2005) 827–848, <https://doi.org/10.1016/j.engfracmech.2004.10.002> Conference on Prospects in Fracture in honor of the 65th Birthday of JG Williams, Imperial Coll London, London, England, Jul 08–09, 2003.
- [12] ASTM International, ASTM B871-01 Standard Test Method for Tear Testing of Aluminum Alloy Products, May 2013. doi:<https://doi.org/10.1520/B0871-01R13>.
- [13] W. Lanning, S. Javaid, C. Muhlstein, Reconciling fracture toughness parameter contradictions in thin ductile metal sheets, *Fatigue Fract. Eng. Mater. Struct.* (2017) 1–16, <https://doi.org/10.1111/ffe.12600>.
- [14] A. Saxena, *Nonlinear Fracture Mechanics for Engineers*, CRC Press, 1998.
- [15] ASTM International, ASTM E345-16 Standard Test Methods of Tension Testing of Metallic Foil, August 2016.
- [16] G. Vander Voort, *Metallography Principles and Practice*, McGraw-Hill Inc., 1984.
- [17] ASTM International, ASTM E112-13 Standard Test Methods for Determining Average Grain Size, October 2013. doi:<https://doi.org/10.1520/E0112-13>.
- [18] I. Dover, J. Eady, R. Gifkins, The tensile deformation of aluminum foil, 1983, pp. 269–274. doi:<https://doi.org/10.1016/B978-1-4832-8423-1.50047-X>.
- [19] J. Chakrabarty, *Theory of Plasticity*, Elsevier, 2006.
- [20] ASM International, Properties of Wrought Aluminum and Aluminum Alloys, ASM International, 1990.
- [21] H. Espinosa, B. Prorok, B. Peng, Plasticity size effects in free-standing submicron polycrystalline FCC films subjected to pure tension, *J. Mech. Phys. Solids* 52 (3) (2004) 667–689, <https://doi.org/10.1016/j.jmps.2003.07.001>.
- [22] H. Hirakata, O. Nishijima, N. Fukuhara, T. Kondo, A. Yonezu, K. Minoshima, Size effect on fracture toughness of freestanding copper nano-films, *Mater. Sci. Eng.* 528 (28) (2011) 8120–8127, <https://doi.org/10.1016/j.msea.2011.07.071>.
- [23] N.F. Mott, A theory of work-hardening of metal crystals, *Philos. Mag.* 43 (346) (1952) 1151–1178, <https://doi.org/10.1080/14786441108521024>.
- [24] J. Friedel, Anomaly in the rigidity modulus of copper alloys for small concentrations, *Philos. Mag.* 44 (351) (1953) 444–448, <https://doi.org/10.1080/14786440408520327>.
- [25] M.S. Blanter, I.S. Golovin, H. Neuhauser, H.R. Sinnning, Internal Friction in Metallic Materials: A Handbook, Springer Series in Materials Science, vol. 90, Springer-Verlag, Berlin, 2007, p. 537, , <https://doi.org/10.1007/978-3-540-68758-0>.
- [26] M.J. Hordon, B.S. Lement, B.L. Averbach, Influence of plastic deformation on expansivity and elastic modulus of aluminum, *Acta Metall.* 6 (6) (1958) 446–453, [https://doi.org/10.1016/0001-6160\(58\)90023-3](https://doi.org/10.1016/0001-6160(58)90023-3).
- [27] C.T. Rosenmayer, F.R. Brotzen, R.J. Gale, Mechanical testing of thin films, *MRS Proc.* 130 (1988) 77, <https://doi.org/10.1557/PROC-130-77>.
- [28] R.W. Hoffman, Nanomechanics of thin films: emphasis: tensile properties, *MRS Proc.* 130 (1988) 295, <https://doi.org/10.1557/PROC-130-295>.
- [29] D. Heinen, H.G. Bohn, W. Schilling, On the mechanical strength of freestanding and substrate-bonded al thin-films, *J. Appl. Phys.* 77 (8) (1995) 3742–3745, <https://doi.org/10.1063/1.360279>.
- [30] D. Heinen, H.G. Bohn, W. Schilling, Internal-friction in freestanding thin al films, *J. Appl. Phys.* 78 (2) (1995) 893–896, <https://doi.org/10.1063/1.358546>.
- [31] M. Hinai, S. Sawaya, H. Masumoto, Effect of cold-working on mechanical damping capacity of al-co alloys, *Mater. Trans.* 34 (4) (1993) 359–363, <https://doi.org/10.2320/matertrans.M2012418>.
- [32] D.T. Read, Y.-W. Cheng, R.R. Keller, J.D. McColsky, Tensile properties of free-standing aluminum thin films, *Scripta Mater.* 45 (5) (2001) 583–589, [https://doi.org/10.1016/S1359-6462\(01\)01067-3](https://doi.org/10.1016/S1359-6462(01)01067-3).
- [33] W.Z. Li, T. Siegmund, An analysis of crack growth in thin-sheet metal via a cohesive zone model 69(18) (2002) 2073–2093. doi:[https://doi.org/10.1016/S0013-7944\(02\)00013-9](https://doi.org/10.1016/S0013-7944(02)00013-9).
- [34] Q.D. Li, G.M. Hua, H. Lu, B. Yu, D.Y. Li, Understanding the effect of plastic deformation on elastic modulus of metals based on a percolation model with electron work function, *JOM* 70 (7) (2018) 1130–1135, <https://doi.org/10.1007/s11883>.
- [35] ASTM International, ASTM D1938-14 Standard Test Method for Tear-Propagation Resistance (Trouser Tear) of Plastic Film and Thin Sheeting by a Single-Tear Method, October 2014. doi:<https://doi.org/10.1520/D1938-14>.